

Evidence for an accreting massive black hole in He 2-10 from adaptive optics integral field spectroscopy

Rogemar A. Riffel,^{1,2*}

¹*Departamento de Física, CCNE, Universidade Federal de Santa Maria, 97105-900, Santa Maria, RS, Brazil*

²*Department of Physics & Astronomy, Johns Hopkins University, Bloomberg Center, 3400 N. Charles St, Baltimore, MD 21218, USA*

Accepted XXX. Received YYY; in original form ZZZ

ABSTRACT

Henize 2–10 is a blue dwarf galaxy with intense star formation and one the most intriguing question about it is whether or not it hosts an accreting massive black hole. We use H and K-band integral field spectra of the inner 130 pc × 130 pc of He 2–10 to investigate the emission and kinematics of the gas at unprecedented spatial resolution. The observations were done using the Gemini Near-Infrared Integral Field Spectrograph (NIFS) operating with the ALTAIR adaptive optics module and the resulting spatial resolutions are 6.5 pc and 8.6 pc in the K and H bands, respectively. Most of the line emission is due to excitation of the gas by photo-ionization and shocks produced by the star forming regions. In addition, our data provide evidence of emission of gas excited by an active galactic nucleus located at the position of the radio and X-ray sources, as revealed by the analysis of the emission-line ratios. The emission lines from the ionized gas in the field present two kinematic components: one narrow with a velocity field suggesting a disk rotation and a broad component due to winds from the star forming regions. The molecular gas shows only the narrow component. The stellar velocity dispersion map presents an enhancement of about 7 km s^{−1} at the position of the black hole, consistent with a mass of $1.5^{+1.3}_{-1.3} \times 10^6 M_{\odot}$.

Key words: galaxies: active – galaxies: kinematics and dynamics – galaxies: dwarf – galaxies: ISM

1 INTRODUCTION

Supermassive black holes (BH), with masses of $10^6 - 10^9 M_{\odot}$, are located at the center of massive galaxies and they are claimed to have a strong impact in the evolution of galaxies (e.g. Magorrian et al. 1998; Di Matteo et al. 2005; Kormendy & Ho 2013; Harrison 2017). While they grow, they produce radiative feedback that shapes the star formation of the host galaxy (e.g. Jeon et al. 2012). Investigate the effect of low-mass ($\sim 10^5 - 10^6 M_{\odot}$) black holes at high-redshift is very difficult from an observational point of view. However, this can be done by observing their analogous in nearby dwarf galaxies (e.g. Filippenko & Sargent 1989; Reines et al. 2011; den Brok et al. 2015), in particular by using integral field spectroscopy (IFS), which allows the mapping of the gas and stellar distribution and kinematics simultaneously (e.g. Vanzani et al. 2008; Cresci et al. 2010, 2017; Brum et al. 2019).

Henize 2–10 (ESO 495- G 021) is one of the most interesting star-forming nearby blue dwarf galaxies, with controversial results regarding the presence of an accreting black hole (Reines et al. 2011; Cresci et al. 2017). It has a very high star formation rate and shows signs of a recent interaction (Kobulnicky et al. 1995; Reines et al. 2011), likely a common event at high z . Indeed, the morphology, metallicity, spectral energy distribution and star-formation rate of a lensed dwarf

starburst at $z = 1.85$ were shown to resemble local starbursting dwarfs (Brammer et al. 2012), making this kind of object a particularly promising early-Universe analogue.

Reines et al. (2011) present optical, near-infrared, radio and X-ray images of He 2–10 obtained with the Hubble Space Telescope (HST), Very Large Array (VLA) and Chandra X-ray Observatory. Based on the ratio between the radio and X-ray luminosities they find that the compact radio source at the dynamical center of the galaxy, and previously reported by Johnson & Kobulnicky (2003), is consistent with an accreting black hole with a mass of $\sim 10^6 M_{\odot}$. Reines et al. (2016) present follow-up X-ray observations of He 2–10 and find that the X-ray source, previously reported, is offset from the radio source and likely an X-ray binary. These deep observations reveal a new X-ray source, co-spatial with the radio source and consistent with a massive BH radiating at $10^{-6} L_{\text{Edd}}$. Very long baseline interferometry observations of He 2–10 at 1.4 GHz reveal a compact non-thermal radio source at the location of the putative accreting BH with a physical scale of $\lesssim 3$ pc × 1 pc (Reines & Deller 2012). However, recent optical integral field spectroscopy (IFS), obtained with the Multi Unit Spectroscopic Explorer (MUSE) on the Very Large Telescope (VLT) at a seeing of $\sim 0''.7$ reveal that the emission-line ratios do not show evidence of an active galactic nucleus (AGN) in He 2–10 (Cresci et al. 2017). These authors, reanalyze the X-ray data and suggest that it is consistent with a supernova remnant origin. The emission-line ratios in the near-infrared

* E-mail: rogemar@ufsm.br

are also consistent with gas excitation due to young stars, and evidence of supernova driven winds are seen in locations co-spatial with non-thermal radio sources (Cresci et al. 2010). Nguyen et al. (2014) use the Gemini-North’s Near-Infrared Integral Field Spectrograph (NIFS) adaptive optics K-band observations of He 2–10 at resolution of $0''.15$ to measure the stellar kinematics by fitting the K-band CO absorption band-heads and place an upper limit to the mass of the BH of $\sim 10^7 M_\odot$. Atacama Large Millimeter Array (ALMA) observations of the cold molecular gas, traced CO(1–0) line, reveal a velocity gradient in molecular gas within the inner 70 pc, consistent with solid body rotation and resulting in a lower limit to the dynamical mass of $2.7 \times 10^6 M_\odot$, which is consistent with the mass of the BH candidate (Imara & Faesi 2019). In addition, Nguyen et al. (2014) report that the Br γ emission at the location of the BH candidate presents a luminosity consistent with that expected from the observed X-ray emission.

Here, we investigate the origin of the near-infrared emission lines from the inner $3'' \times 3''$ of He 2–10 using H and K-band integral field unit data obtained with the Gemini NIFS. The NIFS data present an angular resolution about 6 times better than that of the SINFONI observations previously published by Cresci et al. (2010), thus the NIFS observations are more suitable for a detailed analysis of the nature of the gas emission and to look for signatures of a black hole. This paper is organised as follows. Section 2 presents the description of the data and data reduction procedure, Section 3 presents maps for the emission-line fluxes, line-ratios and kinematics. The results are discussed in Sec. 4 and Sec. 5 presents the conclusions. Through this paper, we adopt the distance to He 2–10 of 9 Mpc (Méndez et al. 1999) and a corresponding physical scale of 43 pc/arcsec.

2 THE DATA AND DATA REDUCTION

We downloaded the NIFS data of He 2–10 from the Gemini Science Archive. The H and K-band observations were done in 2007 April under the program GN-2007A-Q-2 (PI: Usuda) using NIFS together with the ALTitude conjugate Adaptive optics for the InfraRed (ALTAIR). The stellar kinematics and the Br γ emission line flux distribution based on the NIFS K-band data were already published by Nguyen et al. (2014). McGregor et al. (2003) present a technical description of the instrument, which has a square field of view of $\approx 3''.0 \times 3''.0$, divided into 29 slices with an angular sampling of $0''.103 \times 0''.042$. The K-band observations were done using the K_G5605 grating and HK_G0603 filter, while the H band data were obtained using the H_G5605 grating and the JH_G0602 filter. The nominal spectral resolving power for both bands is $R \approx 5290$.

The observations followed the standard Object-Sky-Object dither sequence, with off-source sky positions, and individual exposure times of 300 sec in the K band and 180 sec in the H band. The total on-source exposure times are 45 min and 36 min for the K and H bands, respectively. The H-band spectra are centred at $1.65 \mu\text{m}$, covering the spectral range from 1.48 to $1.80 \mu\text{m}$. The K-band data cover the $2.01\text{--}2.43 \mu\text{m}$ spectral region and the spectra are centred at $2.20 \mu\text{m}$.

We followed the standard steps of NIFS data reduction (e.g., Riffel et al. 2008) using the NIFS package which is part

of GEMINI IRAF package. The data reduction procedure includes the trimming of the images, flat-fielding, cosmic ray rejection, sky subtraction, wavelength and s-distortion calibrations, removal of the telluric absorptions, flux calibration by interpolating a blackbody function to the spectrum of the telluric standard star and construction of data cubes with an angular sampling of $0''.05 \times 0''.05$ for each on-source frame. These individual data cubes were then median combined using a sigma clipping algorithm in order to eliminate bad pixels and taking as reference the position of the continuum peak to perform the astrometry among the single-exposure data cubes.

After the data reduction, we partially apply the data treatment procedure described in Menezes et al. (2014) using PYTHON and IDL routines. First, the data cubes are resampled to $0''.025$ width spaxels using a linear interpolation. Then, we perform a spatial filtering of the data to remove high-frequency noise. We use the BANDPASS_FILTER.PRO IDL routine using a Butterworth spatial filter and adopting a cutoff frequency of 0.15 Nyquist. Finally, data cubes were resampled back to $0''.05$ width spaxels.

In order to estimate the angular resolution, we follow Nguyen et al. (2014) and measure the full-width at half maximum (FWHM) of the flux distribution for the brightest stellar cluster (identified as CLTC1 by these authors) using H and K continuum images. The continuum images were constructed by computing the average of the fluxes within a spectral window of 100 \AA , centred at 1.65 and $2.15 \mu\text{m}$. We measure a $\text{FWHM} \approx 0''.22$ for the K band and $0''.25$ for the H band. Nguyen et al. (2014) measured $\text{FWHM} \approx 0''.19$ for CLTC1 using a high resolution image from HST High Resolution Channel (HRC) obtained through the filter F814W. Thus, the resolution of the NIFS data is $0''.15$ in the K-band and $0''.19$ in the H band. These values correspond to linear scales of 6.5 pc 8.6 pc at the distance of the galaxy. The resulting velocity resolution is $45 \pm 5 \text{ km s}^{-1}$ for both bands, as measured from the FWHM of typical emission lines of the Ar and ArXe lamps spectra used in the wavelength calibration.

Compared to the seeing limited SINFONI data of He 2–10 used by Cresci et al. (2010), the NIFS data present an angular resolution about 6 times better and 75 % (30 %) higher spectral resolution in the H (K) band than theirs. Similarly, the angular resolution of the NIFS data is almost 7 times smaller than that of the optical MUSE data presented by Cresci et al. (2017) and the NIFS velocity resolution is as up to 3 times better than that of the blue part of the MUSE spectra. Thus, the NIFS data can provide a mapping of the gas distribution and kinematics of the inner $130 \text{ pc} \times 130 \text{ pc}$ of He 2–10 in unprecedented detail. On the other hand the instruments used in the studies above present a larger field of view than NIFS, providing information about the physical properties of He 2–10 at larger scales.

3 MEASUREMENTS

We use the *IFSCube* python package¹ to fit the emission line profiles by Gaussian curves. In most locations, the emission lines from the ionized gas present a broad base, besides a

¹ <https://ifscube.readthedocs.io>

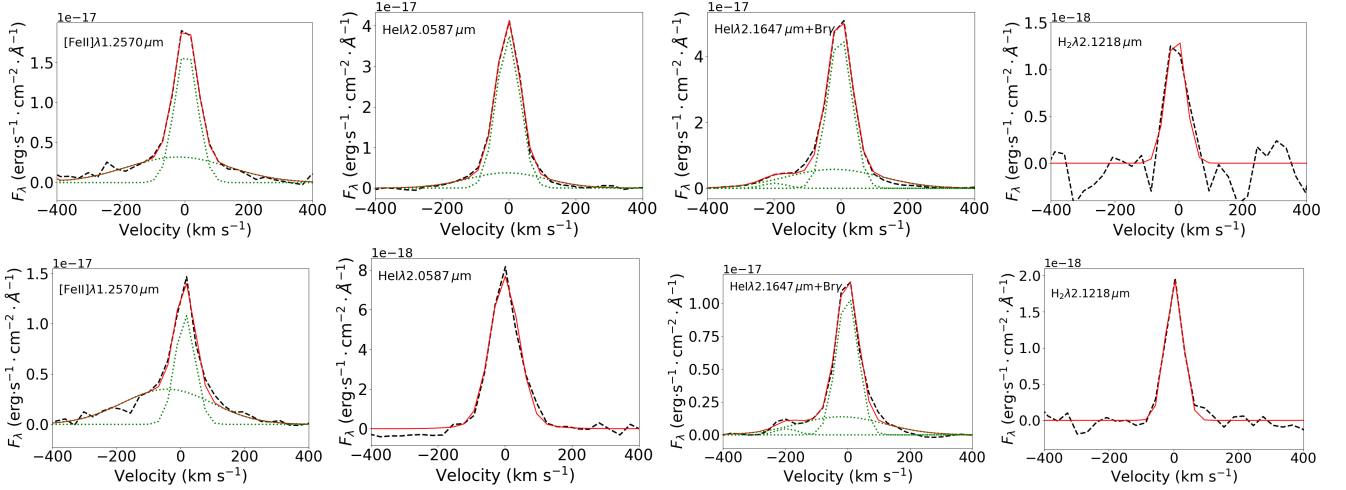


Figure 1. Examples of fits of the emission-line profiles of the $[\text{Fe II}]\lambda 1.6440 \mu\text{m}$, $\text{He I}\lambda 2.0587 \mu\text{m}$, $\text{Br}\gamma$ and $\text{H}_2\lambda 2.1218 \mu\text{m}$ at the position of the peak of $\text{Br}\gamma$ emission (top panels) and at the location of the BH candidate (bottom panels). The observed profiles are shown as dashed black lines, the model as red continuous lines and the green dotted lines show the individual Gaussian components.

narrow component, while the H_2 lines present only the narrow component. The $[\text{Fe II}]\lambda 1.6440 \mu\text{m}$, $\text{He I}\lambda 2.0587 \mu\text{m}$ and $\text{Br}\gamma$ emission lines were fitted using two Gaussian components, while the $\text{H}_2\lambda 2.1218 \mu\text{m}$ is well reproduced by a single Gaussian function in all locations. The velocity dispersion of the broad Gaussian components was constrained to be larger than 100 km s^{-1} , based on visual inspection of the line profiles. If the amplitude of the broad component is smaller than 3 times the standard deviation of the adjacent continuum, the corresponding line profile is fitted by a single Gaussian function. The $\text{Br}12$ emission line, used to estimate the dust extinction, was fitted by a single Gaussian in all locations, as the broad component (if present) is very faint, with amplitude smaller than 3 times the standard deviation of the continuum. In addition, during the fit of the $\text{Br}\gamma$ emission line, we include a Gaussian curve to fit the $\text{He I}\lambda 2.1647 \mu\text{m}$, which is detected and blended with the $\text{Br}\gamma$ in some locations. Examples of the observed line profiles and corresponding fits are shown in Fig. 1.

Although, [Nguyen et al. \(2014\)](#) has already presented stellar kinematics maps for He 2–10 based on the fitting of the K-band NIFS data, our data treatment improves signal-to-noise of the spectra allowing measurements spaxel-by-spaxel, rather than using spatial binned spectra as done by these authors. Thus, we present new measurements for the stellar kinematics based on the treated data cube. The stellar line-of-sight velocity distribution is measured by fitting the CO absorption bandheads at $\sim 2.29\text{--}2.40 \mu\text{m}$ using the Pixel-Fitting PPXF routine ([Cappellari & Emsellem 2004](#); [Cappellari 2017](#)). The spectra of the Gemini library of late spectral type stars observed with the Gemini Near-Infrared Spectrograph (GNIRS) IFU and NIFS ([Winge et al. 2009](#)) are used as spectral templates. This library includes spectra of stars with spectral types from F7 to M5, observed at a very similar spectral resolution than that of the K-band cube of He 2–10.

4 RESULTS

Figure 2 presents the flux distributions for the $[\text{Fe II}]\lambda 1.6440 \mu\text{m}$, $\text{He I}\lambda 2.0587 \mu\text{m}$, $\text{Br}\gamma$ and $\text{H}_2\lambda 2.1218 \mu\text{m}$ emission lines, as well as the K-band continuum. The positions are given relative to the location of the stellar cluster CLTC1 ($\alpha = 08^{\text{h}}36^{\text{m}}15^{\text{s}}.199$, $\delta = -26^{\circ}24'33''.62$), which is co-spatial with the peak of the near-IR continuum ([Reines et al. 2011](#); [Nguyen et al. 2014](#)). The star marks the location of BH candidate ($\alpha = 08^{\text{h}}36^{\text{m}}15^{\text{s}}.12$, $\delta = -26^{\circ}24'34''.1$), defined as the position of the X-ray and compact radio source ([Reines & Deller 2012](#); [Reines et al. 2016](#)). The astrometric uncertainty is $\sim 0''.15$ (the NIFS angular resolution). The $\text{Br}\gamma$ and $\text{He I}\lambda 2.0587 \mu\text{m}$ show similar flux distributions, with emission observed over most of the NIFS field of view for the narrow component, while the broad component is detected mainly to the southeast. The highest flux levels are mainly seen in knots of emission to the south-southeast, which are surrounded by moderate line emission that extends to locations close to the position of the BH candidate. The faintest emission is observed at the north side of the field of view.

The $\text{H}_2\lambda 2.1218 \mu\text{m}$ and the narrow component of the $[\text{Fe II}]\lambda 1.6440 \mu\text{m}$ show overall similar flux distributions and distinct to that of $\text{Br}\gamma$. Strong $[\text{Fe II}]$ and H_2 emission is seen to the southwest and some knots of emission seem to surround the locations of the strongest $\text{Br}\gamma$ emission regions. The highest fluxes for the broad $[\text{Fe II}]$ component is seen between the two knots delineated by the strongest $\text{Br}\gamma$ emission. In addition, a secondary peak is observed at the location of the BH candidate.

Emission-line ratio maps are shown in Figure 3, as well as an $E(B-V)$ map. We estimate the $E(B-V)$ values by

$$E(B-V) = 10.6 \log \left(\frac{F_{\text{Br}\gamma}/F_{\text{Br}12}}{5.29} \right), \quad (1)$$

where $F_{\text{Br}\gamma}$ and $F_{\text{Br}12}$ are the observed fluxes of $\text{Br}\gamma$ and $\text{Br}12$ measured in each spaxel. We use the [Cardelli et al. \(1989\)](#) extinction law, $R_V = 3.1$ and adopt the theoretical ratio between $\text{Br}\gamma$ and $\text{Br}12$ of 5.29, calculated by [Hummer & Storey \(1987\)](#)

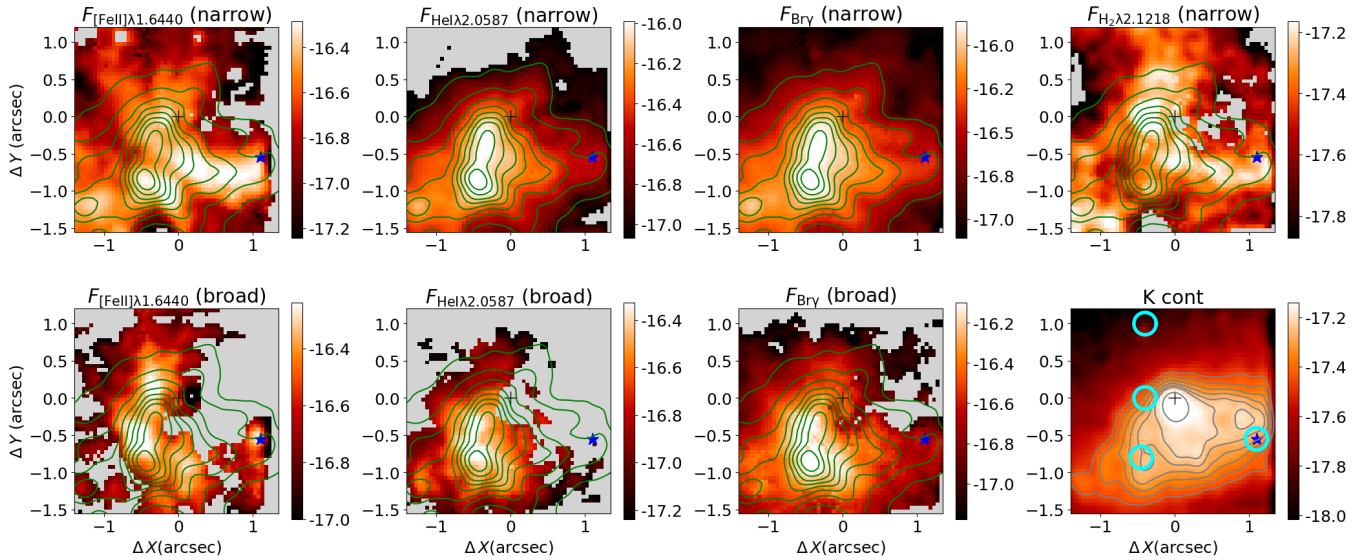


Figure 2. Flux distributions for the narrow and broad line components and K-band continuum image. The green contours overlaid on all maps, but the K-band image, are from the $\text{Br}\gamma$ narrow component, while the gray contours are from the K-band image. The cross marks the position of the stellar cluster CLTC1 and the star shows the position of the BH candidate. The color bars show the fluxes in logarithmic scale of $\text{erg s}^{-1} \text{cm}^{-2} \text{spaxel}^{-1}$ (the size of the spaxels is $0''.05 \times 0''.05$). Gray regions correspond to masked locations where the amplitude of the fitted Gaussian curve is smaller than 3 times the standard deviation of the continuum next to the corresponding emission line. The cyan circles overlaid to the continuum image correspond to the apertures used to extract the spectra discussed in Sec. 5. In all maps, north is up and east is to the left.

for the case B recombination, electron temperature of 10^4 K and electron density of 10^4 cm^{-3} . The resulting $E(B-V)$ map is shown in the bottom-right panel of Fig. 3, with values ranging from ~ 0.5 – 3.0 in good agreement with the range of values presented by Cresci et al. (2010).

The emission-line ratios shown in Fig. 3 are constructed after correction of the line fluxes using the median value of $\langle E(B-V) \rangle = 2.4$ and the extinction law of Cardelli et al. (1989). The $[\text{Fe II}]/\text{Br}\gamma$ and $\text{H}_2/\text{Br}\gamma$ ratios are commonly used to investigate the origin of the $[\text{Fe II}]$ and H_2 emission (Reunanen et al. 2002; Rodríguez-Ardila et al. 2004, 2005; Riffel et al. 2013; Colina et al. 2015). AGN-dominated sources present $-0.3 \leq \log [\text{Fe II}]/\text{Br}\gamma \leq 1.5$ and $-0.3 \leq \log \text{H}_2/\text{Br}\gamma \leq 0.9$, SNe-dominated sources show $0.2 \leq \log [\text{Fe II}]/\text{Br}\gamma \leq 1.2$ and $-0.4 \leq \log \text{H}_2/\text{Br}\gamma \leq 0.4$ and gas excitation by young stars result in $-0.4 \leq \log [\text{Fe II}]/\text{Br}\gamma \leq 0.4$ and $-1.2 \leq \log \text{H}_2/\text{Br}\gamma \leq -0.1$ (Colina et al. 2015). For He 2–10, at most locations $[\text{Fe II}]/\text{Br}\gamma \leq 1.0$ for both narrow and broad components. The broad component shows overall higher ratios than the narrow component and the highest values are seen to the north and in regions close to the location of the BH candidate. Similarly, the $\text{H}_2/\text{Br}\gamma$ shows small values (< 0.2) at most locations and some higher values in the northern side of the field of view. As the He has a higher ionization potential than H, the $\text{He I}/\text{Br}\gamma$ ratio can be used as a tracer of the ionization distribution. From Fig. 3, we note that there is a trend of higher values to the west and at locations close to the BH candidate.

Figure 4 shows the gas velocity maps derived from the centroid of the fitted Gaussian curves, as well as the stellar velocity field derived from the fitting of the CO bands. The observed velocities were corrected to the barycentric velocity and the systemic velocity of the galaxy – $V_s = 872 \pm 6$ (Marquart et al. 2007), is subtracted. The stellar velocity

field shows no sign of rotation with velocities smaller than 25 km s^{-1} and is in agreement with the map derived by Nguyen et al. (2014). On the other hand, the velocity fields for the narrow components of all lines show mostly redshifts to the southwest and blueshifts to the northeast, suggesting a rotation pattern. The maps for the broad components of $[\text{Fe II}]\lambda 1.6440 \mu\text{m}$ and $\text{Br}\gamma$ show blueshifts at most locations, with higher velocities seen for the $[\text{Fe II}]$. The $\text{He I}\lambda 2.0587 \mu\text{m}$ shows velocities close to the systemic velocity of the galaxy.

The velocity dispersion (σ) maps, corrected for the instrumental broadening, are shown in Figure 5. The H_2 shows the smallest σ values and the highest values for the narrow components (50 – 60 km s^{-1}) are seen surrounding the knots of $\text{Br}\gamma$ emission. The σ maps of the broad components of distinct lines show different range of values. The He I shows the smallest values ($\sim 120 \text{ km s}^{-1}$), followed by $\text{Br}\gamma$ ($\sim 140 \text{ km s}^{-1}$) and $[\text{Fe II}]$ presents values of up to 170 km s^{-1} .

5 DISCUSSION

The most intriguing question on He 2–10 is whether or not it hosts an accreting massive black hole. Reines et al. (2011) report that it contains a compact radio source, co-spatial with a hard X-ray source and conclude that the X-ray and radio emission are consistent with an actively accreting black hole with a mass of $\sim 10^6 M_\odot$. Follow up radio (Reines & Deller 2012) and X-ray (Reines et al. 2016) observations provide further evidence of an accreting BH in He 2–10, radiating well below its Eddington limit. Nguyen et al. (2014) derive an upper limit of $\sim 10^7 M_\odot$ for the BH mass, based on the non-detection of increased stellar velocity dispersion at the location of the BH candidate using Gemini NIFS data. Recent

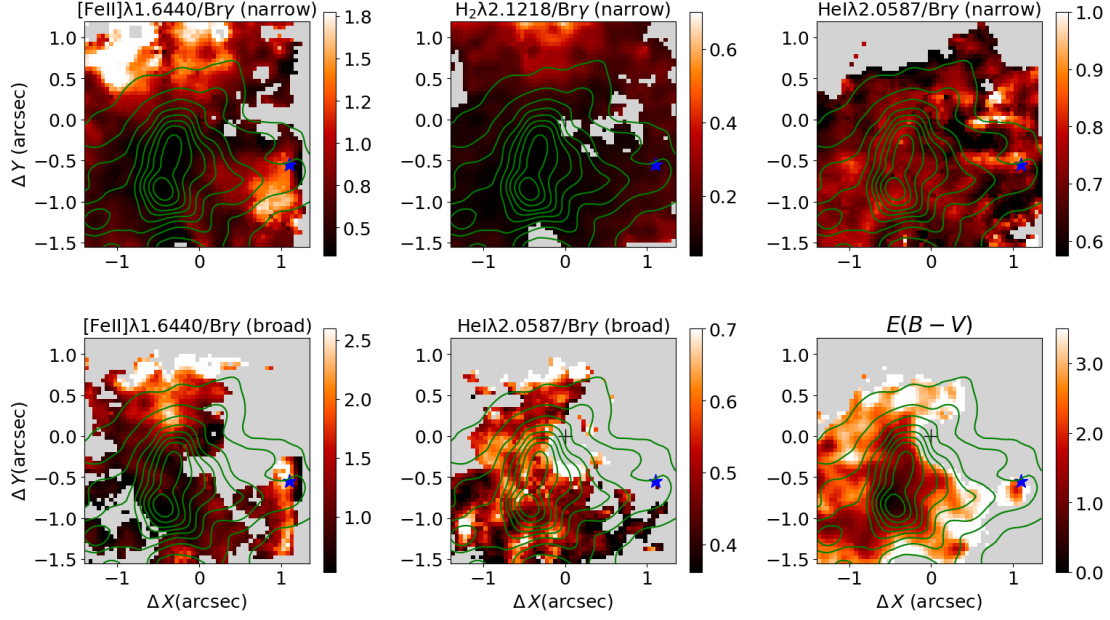


Figure 3. Emission-line ratio maps for He 2–10. Labels are the same as in Fig. 2.

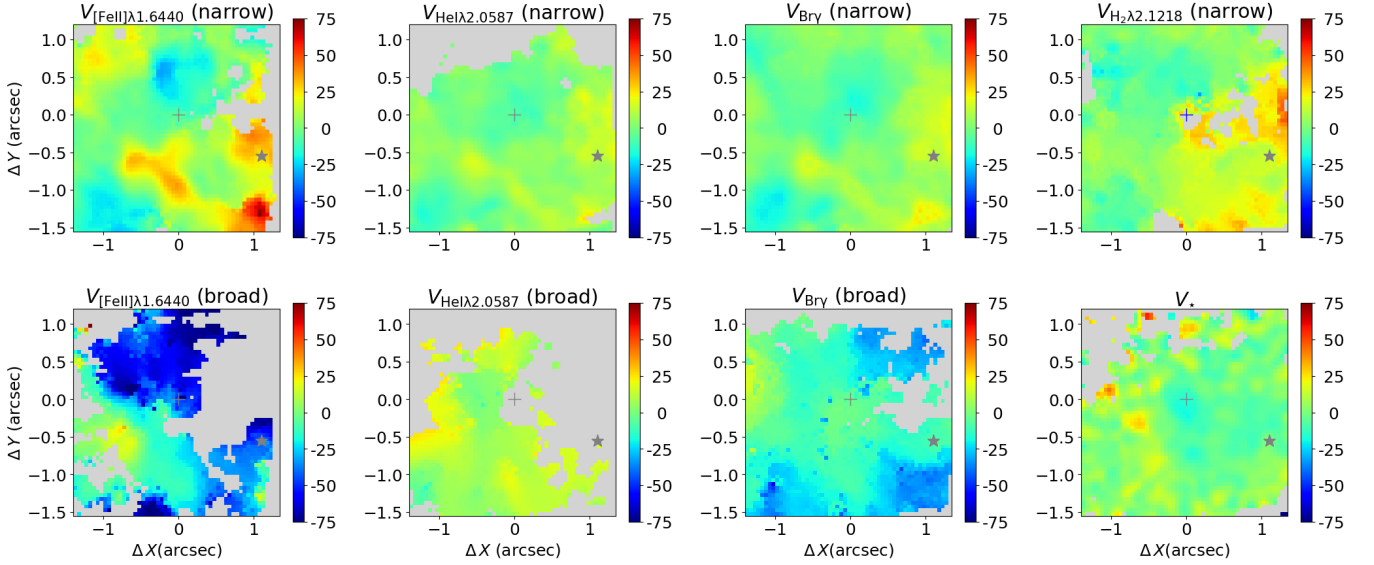


Figure 4. Gas and stellar velocity fields of He 2–10. Labels are the same as in Fig. 2.

ALMA observations reveal a velocity gradient consistent with solid-body rotation and implying in a combined mass of the star clusters and the BH candidate of $\sim 4 \times 10^6 M_\odot$ (Imara & Faesi 2019). However, the optical line ratios of He 2–10 do not show sign of gas ionization by an AGN as obtained using seeing limited IFS with the VLT MUSE instrument (Cresci et al. 2017).

The high angular and spectral resolution data presented here can be used to investigate whether or not He 2–10 hosts an accreting BH. At the location of the BH candidate, we find significant line emission (see Fig. 2), enhanced emission-line ratios (see Fig. 3), consistent with those reported for active galaxies (e.g. Rodríguez-Ardila et al. 2005; Colina et al.

2015). In addition, the stellar velocity dispersion map (Fig. 5) presents slightly higher values at the BH position, providing kinematic support for the presence of a compact object. On the other hand, there are no coronal lines or enhanced continuum due to dust emission in the K-band. However, coronal lines and dust emission are not ubiquitous in type 2 AGN (Riffel et al. 2006, 2009, 2011; Rodríguez-Ardila et al. 2011; Lamperti et al. 2017).

The highest [Fe II]/Br γ values of up to 2.5 are seen close to the location of the BH candidate and to the north of CLTC1, while small values are seen at locations near the knots of Br γ emission, consistent with emission of gas excited by young stellar clusters. A similar behaviour is seen for the H $_2$ /Br γ

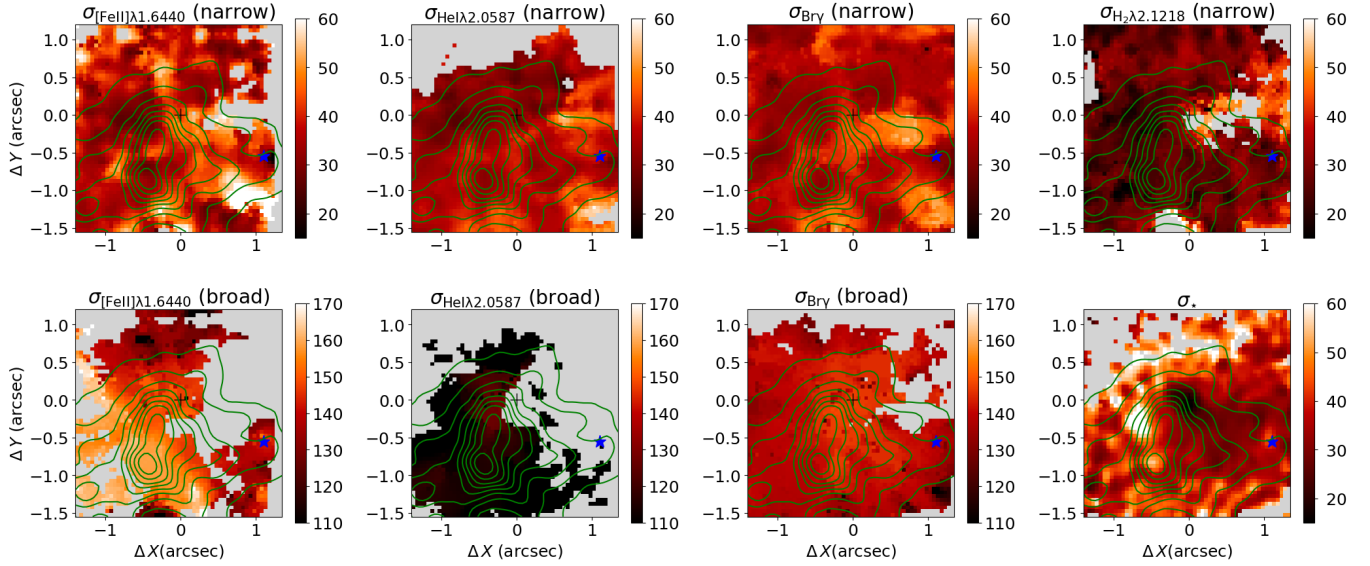


Figure 5. Gas and stellar velocity dispersion maps for He 2–10. Labels are the same as in Fig. 2.

ratio. The high $[\text{Fe II}]/\text{Br}\gamma$ ratios are consistent with an AGN origin, but could also be originated by shocks due to SN winds (Colina et al. 2015). Cresci et al. (2010) do also report enhanced line ratios and suggest that they are due to shocks produced by SN winds. Indeed, the detection of broad line components support the presence of winds associated to the star-forming regions. We find a gradient in the centroid velocity and σ among distinct ionization degrees. The He I shows velocities close to the systemic velocity of the galaxy and the smallest σ values, blueshifts are seen in $\text{Br}\gamma$ and moderate σ values and the highest blueshifts and σ values are seen in $[\text{Fe II}]$. The $\text{He I } \lambda 2.0587 \mu\text{m}$ line traces the emission of the ionized gas with the highest ionization potential among the detected lines, followed by $\text{Br}\gamma$ and $[\text{Fe II}] \lambda 1.6440 \mu\text{m}$. The velocity and σ gradients are consistent with a scenario in which the He I traces the gas emission closer to the young stellar clusters, where the dust has already been swept away by the stellar winds, while the $[\text{Fe II}]$ traces the ‘dustier’ gas farther away from them, where the winds interact with the interstellar medium. Thus, the $[\text{Fe II}]$ broad component traces the most turbulent gas in dustier regions, consistent with the highest σ values and blueshifted velocities, while the redshifted counterpart of the wind is partially extinguished by dust. This scenario is also consistent with the non-detection of a broad component in the H_2 lines, which trace a denser gas phase and the winds may not be powerful enough to significantly affect the kinematics of the dense gas.

As discussed above, the $[\text{Fe II}]/\text{Br}\gamma$ and $\text{H}_2/\text{Br}\gamma$ line ratios alone cannot be used to distinguish between AGN excitation and SN winds as the origin of the line emission. The excitation mechanism of the H_2 lines can be further investigated using the H_2 2–1 $S(1)/1-0 S(1)$ and H_2 1–0 $S(2)/1-0 S(0)$ line ratios (e.g. Mouri 1994; Dors et al. 2012; Riffel et al. 2013). For He 2–10, the lines 1–0 $S(0)$, 1–0 $S(2)$ and 2–1 $S(1)$ are weak and we are not able to measure their fluxes spaxel-by-spaxel. Thus, we extract spectra from four positions with respect to CLTC1: (A) the peak of $\text{Br}\gamma$ emission, at $0''.8$ southeast; (B) the peak of the H_2 emission, at $0''.4$ east; (C) region with

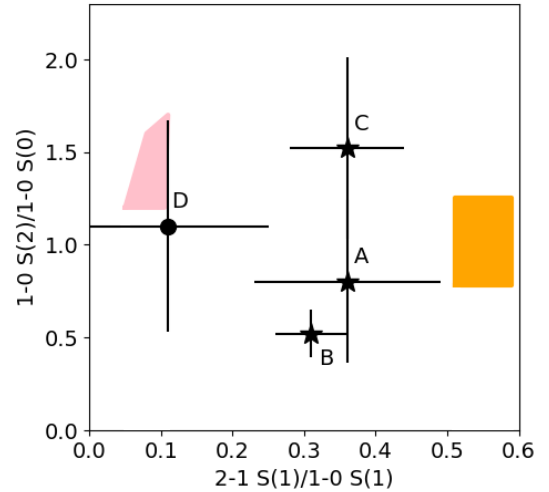


Figure 6. H_2 2–1 $S(1)/1-0 S(1)$ vs. 1–0 $S(2)/1-0 S(0)$ diagram. The points show the observed H_2 emission-line ratios for the positions identified in Fig. 2 (from A to D). The position D corresponds to the location of the BH candidate. The orange rectangle shows the range of values predicted by the non-thermal UV excitation models of Black & van Dishoeck (1987) and the pink polygon indicates the range of values of the AGN photoionization models from Dors et al. (2012) for an ionization parameter $\log U \leq -1.5$.

high $\text{H}_2/\text{Br}\gamma$ and $[\text{Fe II}]/\text{Br}\gamma$ at $1''.1$ north-northeast, and (D) position of the BH candidate ($1''.3$ southwest). The spectra were extracted within circular apertures of $0''.15$ radius, as identified by the cyan circles in Fig. 2, and the corresponding flux ratios are shown in Table 1.

Figure 6 presents the H_2 2–1 $S(1)/1-0 S(1)$ vs. 1–0 $S(2)/1-0 S(0)$ diagram, which can be used to investigate the origin of the H_2 emission. The line ratios at the positions (A), (B) and (C) are seen between the region occupied by the non-thermal UV excitation models of Black & van Dishoeck (1987) – where the H_2 molecule is excited by ultraviolet ab-

sorption, followed by fluorescence – and the region occupied by thermal models (e.g. Riffel et al. 2013) – the bottom left corner of the S(1)/1–0 S(1) vs. 1–0 S(2)/1–0 S(0) diagram. In addition, the observed line ratios from these three positions are close to the observed data points for star-forming galaxies (e.g. Riffel et al. 2013). This suggests that the H₂ emission in these regions is produced mainly by fluorescent excitation through absorption of soft-UV photons from the star-forming regions, but with an additional contribution due to thermal processes (likely shocks due to SN winds), especially for the region (C), that shows the highest 1–0 S(2)/1–0 S(0) ratio and high [Fe II]/Br γ and H₂/Br γ values. Indeed, shock models predict $0.3 < 1-0\text{ S}(1)/1-0\text{ S}(1) < 0.5$ (Hollenbach & McKee 1989), consistent with the observed ratios in these locations. On the other hand, at the position of the BH candidate (D), the observed H₂ line ratios are very close to the values expected for thermal excitation of the H₂. In particular, it is worth noting that the AGN photo-ionization models of Dors et al. (2012) predict values very close to the observed ratio at position D. Thus, we conclude that the data analysed here provide strong evidence to an accreting black hole in He 2–10, contributing to the gas excitation in its vicinity. The enhancement of the [Fe II]/Br γ and He I/Br γ line ratios at the position of the BH further supports this conclusion.

The stellar velocity dispersion map presents a small enhancement at the location of the BH, which can be used to estimate its mass. The median value of σ_* calculated within a circle with radius $R=0''.15$, centred at the position of BH is $\langle \sigma_* \rangle_{\text{BH}} = 39.6 \pm 3.2 \text{ km s}^{-1}$, while for a ring with inner radius of $0''.20$ and outer radius of $0''.30$, the median value is $\langle \sigma_* \rangle_{\text{SP}} = 32.5 \pm 2.9 \text{ km s}^{-1}$. If the slightly enhancement in σ_* at the position of the BH is due its gravitational potential, a rough estimate of BH mass is $1.5^{+1.3}_{-1.3} \times 10^6 M_\odot$ as obtained from the Virial theorem by $M_{\text{BH}} = \frac{2R(\langle \sigma_* \rangle_{\text{BH}}^2 - \langle \sigma_* \rangle_{\text{SP}}^2)}{G}$, where G is the Newton's gravitational constant. This value is in agreement with the expected mass ($\sim 3 \times 10^6 M_\odot$) obtained from the relation between the stellar mass and M_{BH} (Reines & Volonteri 2015) by adopting a stellar mass of $\sim 10^{10} M_\odot$ (Nguyen et al. 2014) and is between the limits calculated by Nguyen et al. (2014) and Imara & Faesi (2019) for He 2–10, as well as between the range of values estimated for BH of NGC 4395, a well known bulgeless dwarf galaxy hosting a Seyfert 1 nucleus (Peterson et al. 2005; den Brok et al. 2015; Brum et al. 2019).

6 CONCLUSION

We use unprecedented high spatial and angular resolution, near-infrared integral field spectra of He 2–10 to investigate the origin of the gas emission and kinematics in the inner $130 \text{ pc} \times 130 \text{ pc}$. These data are consistent with the presence of an accreting massive black hole co-spatial with the location of the compact radio and X-ray source previously reported (e.g. Reines et al. 2016). The main conclusions of this work are:

- Most of the near-infrared line emission is due to gas excited by young stars and shocks, likely due to SN winds. But, at the location of the BH, a contribution of an AGN to the gas excitation is strongly supported by the observed line ratios. The [Fe II] $\lambda 1.6440 \mu\text{m}$ /Br γ and He I $\lambda 2.0587 \mu\text{m}$ /Br γ present

enhanced values at the location of the BH and the H₂ 2–1 S(1)/1–0 S(1) and 1–0 S(2)/1–0 S(0) are consistent with values predicted by AGN photo-ionization models.

- The emission lines from the ionized gas present two kinematic components: (i) a narrow component with $\sigma < 60 \text{ km s}^{-1}$ and velocity field presenting a rotation pattern with redshifts seen to the southwest of the brightest stellar cluster and blueshifts to the northeast of it and a velocity amplitude of 25 km s^{-1} . (ii) A broad component seen mostly in blueshifts and with $\sigma > 100 \text{ km s}^{-1}$, interpreted as being due to winds from the star forming regions. The molecular gas presents only the disk component.

- The stellar velocity field does not present clear signatures of ordered rotation and the stellar velocity dispersion map shows values similar to that of the narrow emission-line component.

- An enhancement of the stellar velocity dispersion from $32.5 \pm 2.9 \text{ km s}^{-1}$ to $39.6 \pm 3.2 \text{ km s}^{-1}$ is observed at the location of the BH, interpreted as being due to motion of stars subjected to the gravitational potential of a black hole with mass of $1.5^{+1.3}_{-1.3} \times 10^6 M_\odot$.

ACKNOWLEDGEMENTS

We thank an anonymous referee for valuable comments that led to improvements in this paper. This study was financed in part by Conselho Nacional de Desenvolvimento Científico e Tecnológico (202582/2018-3, 304927/2017-1 and 400352/2016-8) and Fundação de Amparo à pesquisa do Estado do Rio Grande do Sul (17/2551-0001144-9 and 16/2551-0000251-7).

Based on observations obtained at the Gemini Observatory (acquired through the Gemini Observatory Archive and processed using the Gemini IRAF package), which is operated by the Association of Universities for Research in Astronomy, Inc., under a cooperative agreement with the NSF on behalf of the Gemini partnership: the National Science Foundation (United States), National Research Council (Canada), CONICYT (Chile), Ministerio de Ciencia, Tecnología e Innovación Productiva (Argentina), Ministério da Ciência, Tecnologia e Inovação (Brazil), and Korea Astronomy and Space Science Institute (Republic of Korea). This research has made use of NASA's Astrophysics Data System Bibliographic Services. This research has made use of the NASA/IPAC Extragalactic Database (NED), which is operated by the Jet Propulsion Laboratory, California Institute of Technology, under contract with the National Aeronautics and Space Administration.

REFERENCES

- Black J. H., van Dishoeck E. F., 1987, *ApJ*, **322**, 412
- Brammer G. B., et al., 2012, *ApJ*, **758**, L17
- Brum C., et al., 2019, *MNRAS*, **486**, 691
- Cappellari M., 2017, *MNRAS*, **466**, 798
- Cappellari M., Emsellem E., 2004, *PASP*, **116**, 138
- Cardelli J. A., Clayton G. C., Mathis J. S., 1989, *ApJ*, **345**, 245
- Colina L., et al., 2015, *A&A*, **578**, A48
- Cresci G., Vanzì L., Sauvage M., Santangelo G., van der Werf P., 2010, *A&A*, **520**, A82

Table 1. H₂ 2–1 S(1)/1–0 S(1) and 1–0 S(2)/1–0 S(0) emission line ratios measured the four positions identified as cyan circles in Fig. 2.

Position/Ratio	A (Peak Br γ)	B (Peak H ₂)	C (High H ₂ /Br γ)	D (BH candidate)
2–1 S(1)/1–0 S(1)	0.36 ± 0.13	0.31 ± 0.05	0.36 ± 0.08	0.11 ± 0.14
1–0 S(2)/1–0 S(0)	0.80 ± 0.44	0.52 ± 0.13	1.52 ± 0.49	1.10 ± 0.57

- Cresci G., Vanzi L., Telles E., Lanzuisi G., Brusa M., Mingozzi M., Sauvage M., Johnson K., 2017, *A&A*, **604**, A101
- Di Matteo T., Springel V., Hernquist L., 2005, *Nature*, **433**, 604
- Dors Oli L. J., Riffel R. A., Cardaci M. V., Hägele G. F., Krabbe Á. C., Pérez-Montero E., Rodrigues I., 2012, *MNRAS*, **422**, 252
- Filippenko A. V., Sargent W. L. W., 1989, *ApJ*, **342**, L11
- Harrison C. M., 2017, *Nature Astronomy*, **1**, 0165
- Hollenbach D., McKee C. F., 1989, *ApJ*, **342**, 306
- Hummer D. G., Storey P. J., 1987, *MNRAS*, **224**, 801
- Imara N., Faesi C. M., 2019, *ApJ*, **876**, 141
- Jeon M., Pawlik A. H., Greif T. H., Glover S. C. O., Bromm V., Milosavljević M., Klessen R. S., 2012, *ApJ*, **754**, 34
- Johnson K. E., Kobulnicky H. A., 2003, *ApJ*, **597**, 923
- Kobulnicky H. A., Dickey J. M., Sargent A. I., Hogg D. E., Conti P. S., 1995, *AJ*, **110**, 116
- Kormendy J., Ho L. C., 2013, *ARA&A*, **51**, 511
- Lamperti I., et al., 2017, *MNRAS*, **467**, 540
- Magorrian J., et al., 1998, *AJ*, **115**, 2285
- Marquart T., Fathi K., Östlin G., Bergvall N., Cumming R. J., Amram P., 2007, *A&A*, **474**, L9
- McGregor P. J., et al., 2003, Gemini near-infrared integral field spectrograph (NIFS). Proceedings of the SPIE, pp 1581–1591, doi:10.1117/12.459448
- Méndez D. I., Esteban C., Filipović M. D., Ehle M., Haberl F., Pietsch W., Haynes R. F., 1999, *A&A*, **349**, 801
- Menezes R. B., Steiner J. E., Ricci T. V., 2014, *MNRAS*, **438**, 2597
- Mouri H., 1994, *ApJ*, **427**, 777
- Nguyen D. D., Seth A. C., Reines A. E., den Brok M., Sand D., McLeod B., 2014, *ApJ*, **794**, 34
- Peterson B. M., et al., 2005, *ApJ*, **632**, 799
- Reines A. E., Deller A. T., 2012, *ApJ*, **750**, L24
- Reines A. E., Volonteri M., 2015, *ApJ*, **813**, 82
- Reines A. E., Sivakoff G. R., Johnson K. E., Brogan C. L., 2011, *Nature*, **470**, 66
- Reines A. E., Reynolds M. T., Miller J. M., Sivakoff G. R., Greene J. E., Hickox R. C., Johnson K. E., 2016, *ApJ*, **830**, L35
- Reunanen J., Kotilainen J. K., Prieto M. A., 2002, *MNRAS*, **331**, 154
- Riffel R., Rodríguez-Ardila A., Pastoriza M. G., 2006, *A&A*, **457**, 61
- Riffel R. A., Storch-Bergmann T., Winge C., McGregor P. J., Beck T., Schmitt H., 2008, *MNRAS*, **385**, 1129
- Riffel R., Pastoriza M. G., Rodríguez-Ardila A., Bonatto C., 2009, *MNRAS*, **400**, 273
- Riffel R., Riffel R. A., Ferrari F., Storch-Bergmann T., 2011, *MNRAS*, **416**, 493
- Riffel R., Rodríguez-Ardila A., Aleman I., Brotherton M. S., Pastoriza M. G., Bonatto C., Dors O. L., 2013, *MNRAS*, **430**, 2002
- Rodríguez-Ardila A., Pastoriza M. G., Viegas S., Sigut T. A. A., Pradhan A. K., 2004, *A&A*, **425**, 457
- Rodríguez-Ardila A., Riffel R., Pastoriza M. G., 2005, *MNRAS*, **364**, 1041
- Rodríguez-Ardila A., Prieto M. A., Portilla J. G., Tejeiro J. M., 2011, *ApJ*, **743**, 100
- Vanzi L., Cresci G., Telles E., Melnick J., 2008, *A&A*, **486**, 393
- Winge C., Riffel R. A., Storch-Bergmann T., 2009, *ApJS*, **185**, 186
- den Brok M., et al., 2015, *ApJ*, **809**, 101

This paper has been typeset from a T_EX/L^AT_EX file prepared by the author.